

A comparative study on the pore structure of alkali-activated fly ash evaluated by mercury intrusion porosimetry, N₂ adsorption and image analysis

Ma, Y.; Wang, G.; Ye, G.; Hu, J.

DOI

[10.1007/s10853-017-1965-x](https://doi.org/10.1007/s10853-017-1965-x)

Publication date

2018

Document Version

Final published version

Published in

Journal of Materials Science

Citation (APA)

Ma, Y., Wang, G., Ye, G., & Hu, J. (2018). A comparative study on the pore structure of alkali-activated fly ash evaluated by mercury intrusion porosimetry, N₂ adsorption and image analysis. *Journal of Materials Science*, 53(8), 5958–5972. <https://doi.org/10.1007/s10853-017-1965-x>

Important note

To cite this publication, please use the final published version (if applicable). Please check the document version above.

Copyright


Other than for strictly personal use, it is not permitted to download, forward or distribute the text or part of it, without the consent of the author(s) and/or copyright holder(s), unless the work is under an open content license such as Creative Commons.

Takedown policy

Please contact us and provide details if you believe this document breaches copyrights. We will remove access to the work immediately and investigate your claim.



A comparative study on the pore structure of alkali-activated fly ash evaluated by mercury intrusion porosimetry, N₂ adsorption and image analysis

Y. Ma^{1,2,*} , G. Wang¹, G. Ye^{3,4}, and J. Hu^{5,*}

¹Guangzhou University - Tamkang University Joint Research, Center for Engineering Structure Disaster Prevention and Control, Guangzhou University, Guangzhou 510006, People's Republic of China

²Centre for Future Materials, Faculty of Health, Engineering and Sciences, University of Southern Queensland, Toowoomba, Australia

³Department Materials and Environment, Faculty of Civil Engineering and Geosciences, Delft University of Technology, Delft, The Netherlands

⁴Department of Structural Engineering, Ghent University, Ghent, Belgium

⁵School of Materials Science and Engineering, South China University of Technology, Guangzhou 510640, People's Republic of China

Received: 10 October 2017

Accepted: 22 December 2017

Published online:

9 January 2018

© Springer Science+Business Media, LLC, part of Springer Nature 2018

ABSTRACT

In this study, the pore structure of alkali-activated fly ash (AAFA) pastes characterized by different techniques, including mercury intrusion porosimetry (MIP), nitrogen adsorption and image analysis (based on backscattered electron images), was evaluated and compared critically. The degree of reaction of fly ash in AAFA pastes was derived from image analysis. It was found that due to a significant “ink-bottle” effect, the pore diameter of capillary pores derived from MIP was two orders of magnitude smaller than the size determined by image analysis. MIP and nitrogen adsorption results showed different peaks corresponding to the gel pores of AAFA pastes. Based on the experimental results, image analysis is regarded as a reliable technique for the characterization of large pores (> 1 μm) in AAFA pastes. Nitrogen adsorption is more suitable to characterize small pores (< 0.1 μm) in AAFA than MIP, and MIP data should be carefully interpreted, preferably in combination with other characterization techniques.

Introduction

Alkali-activated materials (AAM) are a class of solid materials prepared by the reaction between aluminosilicate powders and alkaline solution. The

industrial by-product, e.g. fly ash, is widely applied for the synthesis of alkali-activated materials. The reaction product of alkali-activated fly ash (AAFA) is a three-dimensional sodium aluminosilicate gel [1]. Such gel is chemically and morphologically different

Address correspondence to E-mail: yuwei.ma@hotmail.com; msjiehu@scut.edu.cn

from the hydrated calcium silicate (CSH) gel in cement-based materials. Due to its substantial reduction in CO₂ emission [2], as well as superior mechanical strength and excellent durability under aggressive environment, AAFA has gained increasing attention in the last few decades. The reaction kinetics, effect of different activators and curing condition on the reaction product and microstructure of AAFA have been investigated by numerous studies [3, 4].

Similar to conventional cement-based materials, AAFA also presents an inherently porous feature. It covers a broad pore size range from several nanometres to hundreds of micrometres. It is known that the pore volume and the pore size distribution are significantly important in determining the mechanical property and durability of AAFA. Aggressive ions (e.g. Cl⁻, CO₃²⁻, SO₄²⁻, etc.) may enter the AAFA paste/mortar/concrete through these pores and lead to the degradation of the material. In addition, the shrinkage (both autogenous and drying shrinkage) is also related to the pore structure, especially the mesopores in AAFA. Therefore, a comprehensive understanding of the pore structure of AAFA is very important for the evaluation and further prediction of the service life of AAFA. So far, numerous experimental techniques have been applied to evaluate the pore structure of AAFA. Among these techniques, mercury intrusion porosimetry (MIP) is the most preferred and efficient method [5]. MIP is able to determine nearly the whole range of pore sizes that is needed to characterize cement paste and AAFA (from 6 nm to 350 μm in this study). However, it is argued that the results derived from MIP cannot depict the actual pore shape and pore size distribution of cement-based materials [5]. For example, the presence of “ink-bottle pores” will lead to an overestimation on the volume of fine pores and an underestimation of the volume of large pores [6]. Further, in some cases, the high pressure employed during the intrusion process may lead to damage of pores, resulting in inaccurate results [7, 8]. Nitrogen adsorption is another technique which has been widely employed to characterize the pore structure of porous material [5]. On the basis of the adsorbed gas amount and corresponding relative gas pressure, the internal surface area of pores, as well as pore size distribution, can be obtained by using Brunauer–Emmett–Teller (BET) theory and Barrett–Joyner–Halenda (BJH) model [9], respectively.

Nitrogen adsorption is able to distinguish pore size in the range of 0.3–300 nm [10] (from 2 to 100 nm in this study). Within this range, the analysis of pores in the nanoscale is possible. However, nitrogen adsorption can only access to open pores; besides, the cylindrical pore model is assumed for the interpretation of the data [11], a condition which is never fulfilled for cement-based materials and AAFA in the present study. Furthermore, the small range of pore sizes determined by nitrogen adsorption cannot provide enough information about pores existed in AAFA. Besides the above two techniques, image analysis based on backscattered electron (BSE) images is a promising way to analyse the pore structure of AAFA. It allows the characterization of pore geometry to be analysed from a real image of the material. In addition, the degree of the reaction of AAFA can also be derived by image analysis [12]. However, the minimum size of pores that can be distinguished by ESEM is limited (normally > 100 nm) and mainly depends on the magnification and resolution of the image [13], which will affect the accuracy of reaction degree.

The three techniques introduced above (i.e. MIP, nitrogen adsorption and image analysis) are all capable to characterize the pore structure of AAFA. Each technique has its advantages and limitations. It is difficult to obtain the full image of pore structure of AAFA by using only one single technique. Combinations of these techniques as well as a careful interpretation of the experimental data are needed. To this end, in this study the pore structure data derived from different techniques (i.e. MIP, nitrogen adsorption and image analysis) were investigated and compared critically. The suitability of each technique in characterizing the pores in AAFA was evaluated. Further, the degree of the reaction of AAFA with different activator content (SiO₂ and Na₂O content) and different curing age was also investigated by BSE images coupled with image analysis.

Materials and methods

Materials and mixture proportions of AAFA

Low-calcium fly ash, Class F according to ASTM C 618, obtained from The Netherlands, was used in this study. Class F fly ash was commonly used for the

preparation of AAFA. The chemical composition of the fly ash is shown in Table 1. The main chemical constituents of the fly ash were SiO₂ and Al₂O₃, and the main crystalline compounds were quartz (SiO₂) and mullite (3Al₂O₃·2SiO₂). The amorphous content of fly ash, determined by chemical dissolution treatment (EN 196, Part 2), was 69%. The mean particle size of the used fly ash was 21.46 μm.

The alkali activators were obtained by mixing sodium silicate solution (Na₂O: 8.25 wt%, SiO₂: 27.50 wt%) with sodium hydroxide (analytical grade, > 98% purity) and distilled water. Na₂O and SiO₂ contents supplied by the activator were 1.0 mol or 1.5 mols per 1000 g fly ash, as described in Table 2. Alkali activators were previously optimized to present good mechanical property after curing at 40 °C for 7 and 28 days [14] (Table 2). The compressive strength of AAFA pastes was carried out on 40 × 40 × 40 mm cubes, according to NEN-EN-196-1 (Methods of testing cement-Part 1: Determination of strength). For each mixture, at least three replicates were tested. The water/binder ratio was maintained at 0.35. All alkali activators were prepared 1 day before sample preparation.

For sample preparation, fly ash was mixed with the activator in a mixer for 4 min. Sealed curing condition was applied on AAFA to minimize drying and carbonation. In this study, fresh AAFA paste was poured into a polyethylene (PE) bottle which has a diameter of 35 mm and height of 65 mm. The bottles were vibrated for 1 min to remove air bubbles and then sealed with a screw cap. The sealed specimens were cured at 40 °C for 7 and 28 days. At each curing

age, specimens were crushed into small pieces (1–2 cm³). More detail information about sample casting and curing was previously reported in [15] (Section 1.6.2 Casting and curing). Liquid nitrogen was used to stop reaction of the specimens. After that, these specimens were then dried at – 28 °C in a vacuum freeze-dryer to remove the free water. Such drying method allowed the remaining water in samples transforming into ice microcrystal and being removed by sublimation while the change of microstructure was not significant [16].

Mercury intrusion porosimetry (MIP)

Micromeritics Poresizer 9500 was used for MIP measurement in this study. MIP test was conducted in two stages: the first stage is low pressure stage, with the pressure running from 0 to 0.0036 MPa; and the second stage is high pressure stage, with the pressure running from 0.0036 to 210 MPa, followed by an extrusion process running from 210 to 0.14 MPa. The diameter of pores intruded by mercury at each pressure step was calculated by using Washburn equation [17] as follows:

$$D = \frac{-4\gamma \cos \theta}{P} \quad (1)$$

where D is the pore diameter of materials, γ is the surface tension of mercury (0.485 N/m used here), θ is the contact angle between mercury and sample surface (132° according to the previous study [18]); and P is the applied pressure. In this study, the pore size ranging from 350 to 0.007 μm can be detected by using MIP.

Table 1 Chemical composition and physical properties of the fly ash used in this study

| Oxide | SiO ₂ | Al ₂ O ₃ | Fe ₂ O ₃ | CaO | MgO | K ₂ O | Na ₂ O | TiO ₂ | P ₂ O ₅ | SO ₃ | L.I. |
|-----------------------|------------------|--------------------------------|--------------------------------|------|------|------------------|-------------------|------------------|-------------------------------|-----------------|------|
| Weight (%) | 48.36 | 31.36 | 4.44 | 7.14 | 1.35 | 1.64 | 0.72 | 1.24 | 1.90 | 1.18 | 4.89 |
| L.I. loss on ignition | | | | | | | | | | | |

Table 2 Mixture proportion and compressive strength of AAFA mixtures

| Sample (SiO ₂ –Na ₂ O) | Fly ash (g) | SiO ₂ (mol) ^a | Na ₂ O (mol) ^a | H ₂ O (g) | Compressive strength at 7 days (MPa) ^b | Compressive strength at 28 days (MPa) ^b |
|--|-------------|-------------------------------------|--------------------------------------|----------------------|---|--|
| 1.0–1.0 | 1000 | 1.0 | 1.0 | 350 | 34 | 45 |
| 1.0–1.5 | 1000 | 1.0 | 1.5 | 350 | 45 | 76 |
| 1.5–1.5 | 1000 | 1.5 | 1.5 | 350 | 52 | 66 |

^aContent in the activator

^bCuring at 40 °C

Nitrogen adsorption

In this study, the equipment used for nitrogen adsorption tests was Gemini VII 2390. Nitrogen adsorption is able to detect the small pores (from 0.3 to 300 nm [19]) in porous materials. Within this range, the analysis of pores in the nanoscale is possible. At each curing age (7 and 28 days, respectively), dried specimens (dried by freeze-dry method) were crushed into small pieces (about 1 mm³) and then submitted to the nitrogen adsorption tests. The relative pressure (p/p_0) ranging from 0.05 to 0.98 was recorded, corresponding to the pore size in the range of 2–100 nm. Barrett–Joyner–Halenda (BJH) [20] model was employed to derive the pore size distribution curve from the nitrogen adsorption data.

Image analysis based on environmental scanning electron microscope (ESEM)

Sample preparation for ESEM observation

Image analysis using BSE requires a well-polished surface for optimal analysis. Sample preparation for ESEM observations in this study included epoxy impregnation, cutting, grinding and polishing. In order to obtain a BSE image with high quality, specimens need to be well grinded and polished. To prepare the samples, the surfaces of the specimens were first grinded on the middle-speed lap wheel with different SiC papers (3 min for each SiC paper): p320, p500, p800, p1200 and p4000. The samples were then polished on a lap wheel with different finer grades of diamond abrasive cloth: 6, 3, 1 and 0.25 μm . The final polishing was carried out on a low-relief polishing cloth. For the grinding and polishing procedure, ethanol was used as the lubricant. Afterwards, the specimens were immersed in an ultrasonic bath to remove the dust and diamond particles left on the specimen surface (more details about the sample preparation procedure can be found in [16]).

Image acquisition

At the curing age of 7 and 28 days, specimens were examined by ESEM (Philips-XL30) with backscattering electron (BSE) mode. The acceleration voltage was 15–20 kV (as long as a good image was obtained) and the water vapour pressure was kept constant at

1.0 Torr. The physical size of each image was 496 μm in length and 376 μm in width. The magnification of each image was kept constant at 250 \times , and the image size was 1424 \times 968 pixel. By calculation, the resolution of the image was about 0.39 μm /pixel.

Image analysis technique

Image analysis technique was applied to quantitatively characterize the pore size distribution and degree of reaction (based on the alteration of area ratio corresponding to unreacted particles) from BSE images. BSE image was acquired in 8 bits; and 256 grey-level values were included in the image, ranging from 0 (black) to 255 (white). In the image, the image contrast was closely related to the element composition of different phases [21]: those with a higher atomic number were brighter, and those with a lower atomic number were darker. Therefore, according to the grey-level histogram of the image, different phases in AAFA can be distinguished. The image analysis was based on the grey-level distribution of all pixels in the image. Figure 1 shows the original BSE image and corresponding grey-level histogram of a typical AAFA paste sample. Unreacted fly ash particles presented the highest average atomic number; thus, the peak corresponded to the right side of the grey-level histogram (Fig. 1b) represented the phase of unreacted fly ash particles. The peak in the middle in the grey-level histogram was reaction products. The pores were distinguished as black in the BSE image, corresponding to the left peak as shown in Fig. 1b.

BSE images can be analysed to obtain the volume fraction and size distribution of different phases in AAFA paste, based on image segmentation methods. When fly ash particles are randomly distributed in the system, the area fractions and distribution of the phases obtained from a 2D image are approximately equal to the 3D real structure [22].

In the simplest situation, by choosing a proper grey-level value as the threshold, the segmentation can be performed based on the histogram. However, due to the intermixing of grey levels of different phases, it is often difficult to select an appropriate threshold value. In the present study, the extraction of the pores from the BSE images was performed by using some techniques included in most commonly used image analysis software. Figure 2 shows the flow chart of the algorithm.

Figure 1 SEM-BSE image ($\times 250$) of a typical AAFA paste sample (a) and corresponding grey-level histogram (b).

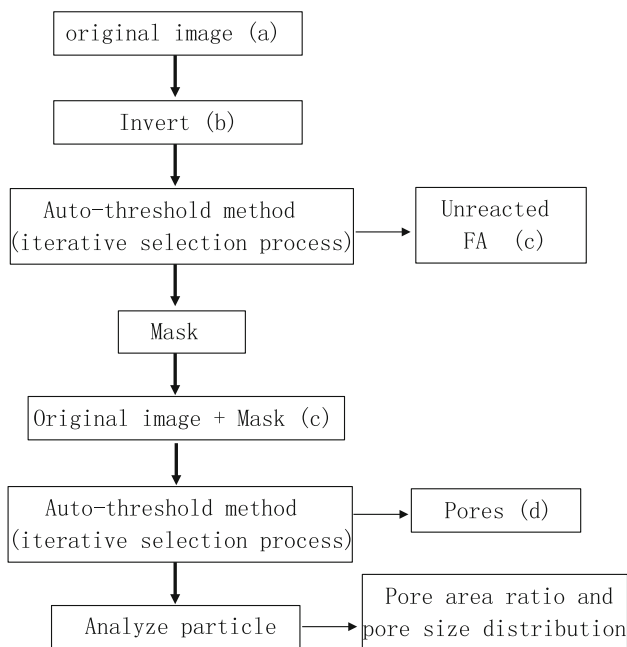
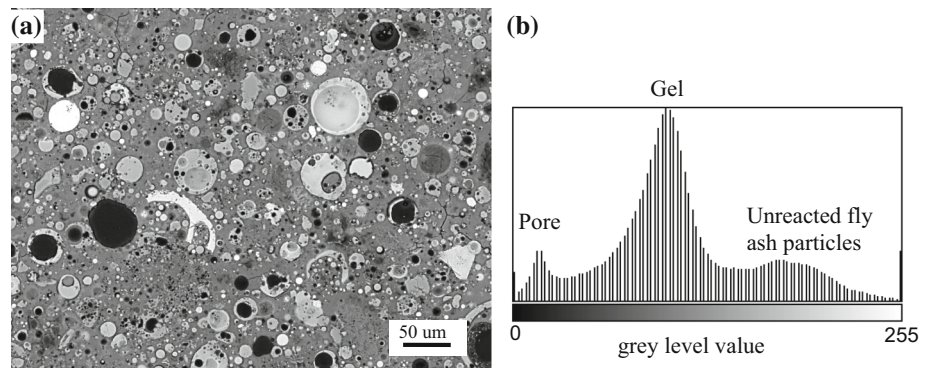


Figure 2 Image processing sequence. Letters (a–d) refer to the steps shown in Fig. 3.

In this approach, unreacted fly ash particles were first extracted from the BSE image. The iterative selection process (also known as Isodata algorithm [23]) was applied to choose an optimum threshold value automatically. In this process, the image was divided into the object and background by choosing an initial threshold. Afterwards, the average values of the pixels at or below the threshold and pixels above were computed, respectively. The above two average values were computed, and the threshold was incremented. The process was repeated until the threshold was larger than the composite average value [23]. Figure 3c presents a binary image of the unreacted fly ash after the auto-threshold method. The binary image of the unreacted fly ash was then

used as a mask on the original image to remove the pixels remaining in the image that belongs to the unreacted fly ash. Afterwards, the iterative selection process was applied on the obtained image to segment pores. Figure 3d is an obtained image consisted of only the pores based on which it is easy to calculate the pore surface area and pore size distribution. Figure 4 shows the pore size distribution curve of one AAFA mixture derived from the image analysis. For each mixture, at least 12 images (95% degree of confidence could be achieved [16]) were used for image analysis; the resulting pore size distribution curve was the average data derived from 12 image analysis. The pore size determined by image analysis was between $0.6 \mu\text{m}$ to around $150 \mu\text{m}$ in this study.

The degree of reaction of fly ash, $\alpha(t)$, is calculated by subtracting the content of unreacted fly ash and dividing it by the initial fly ash content:

$$\alpha(t) = (1 - U_t/U_0) \times 100\% \quad (2)$$

where U_t is the volume fraction of unreacted fly ash particles at the age t (obtained from image analysis); U_0 is the initial volume fraction of fly ash particles. The initial volume fraction of fly ash particles was calculated based on the initial activating solution/fly ash volume ratio. For the mixtures $\text{SiO}_2\text{--Na}_2\text{O} = 1.0\text{--}1.0$, $1.0\text{--}1.5$ and $1.5\text{--}1.5$ pastes, the volume of the activating solution was measured as 0.360, 0.358 and 0.368 L (mixed with 1 kg fly ash), respectively. The measured density of the used fly ash was 2.44 g/cm^3 , which was corresponded to a volume of 0.41 L of 1 kg fly ash. Thus, the initial volume fraction of fly ash for mixtures 1.0–1.0, 1.0–1.5 and 1.5–1.5 was 53.2, 53.4 and 52.7%, respectively.

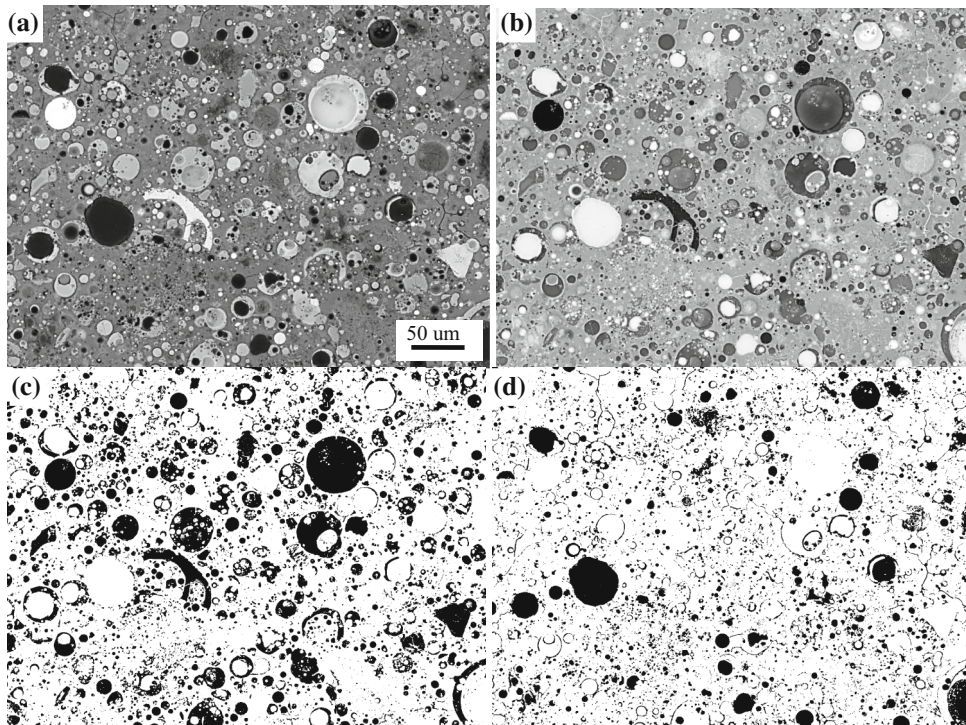
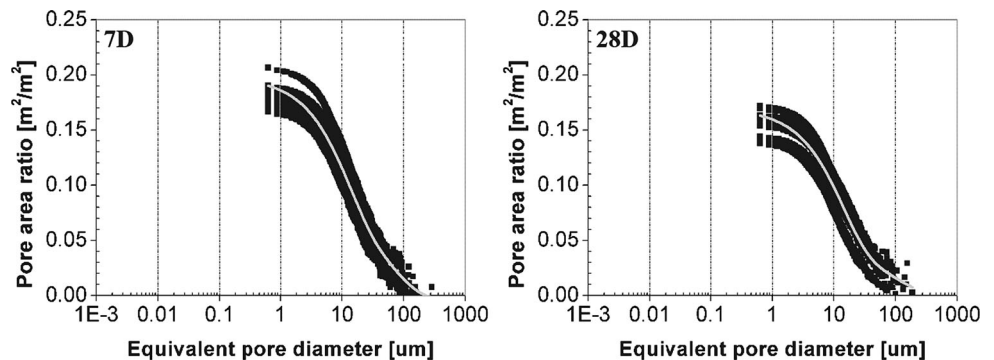


Figure 3 Images after different segmentation steps. **a** Original image; **b** invert image; **c** binary image of unreacted fly ash; **d** binary image of pores.

Figure 4 Pore size distribution of one AAFA mixtures (1.0–1.0) at 7 and 28 days, derived from image analysis.



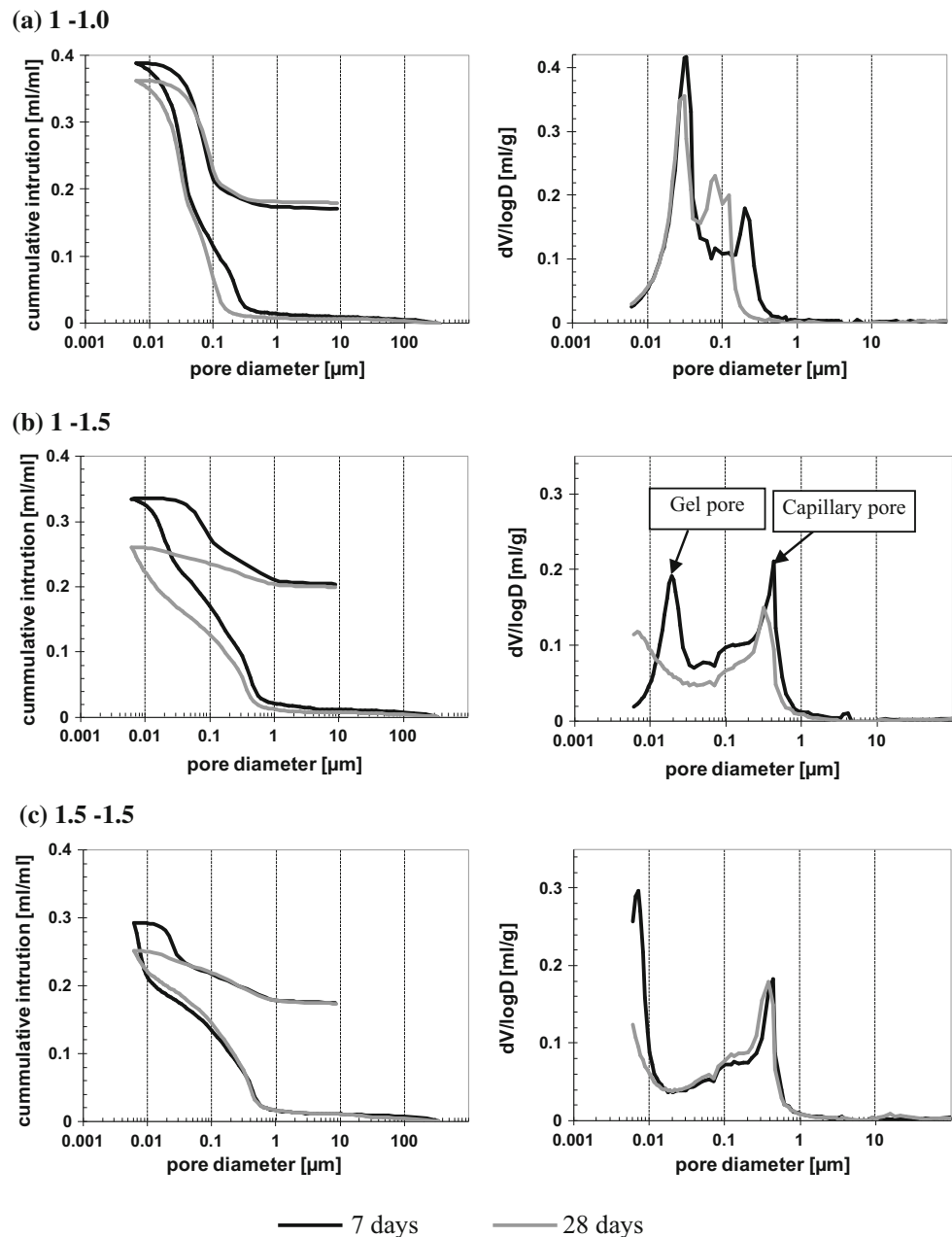
Results and discussion

Pore structure of AAFA pastes determined by MIP

Figure 5 shows the pore size distribution and differential curves of AAFA pastes prepared with different SiO_2 and Na_2O content in activator at the curing age of 7 and 28 days. The differential curves of AAFA generally show two peaks, representing two types of pores: the first peak (e.g. left in Fig. 5b), in a pore diameter range of several nm to $0.04\ \mu\text{m}$, corresponded to the gel pores; the second peak (e.g. right

in Fig. 5b), in a pore size between 0.1 and $1\ \mu\text{m}$, was corresponding to the capillary pores of AAFA. As observed from Fig. 5, the total porosity of all investigated AAFA samples decreased from 7 to 28 days. Meanwhile, both peaks corresponding to the thresholds of gel pores and capillary pores (in the differential curves in Fig. 5) shifted to a smaller pore diameter at later curing age, indicating a denser microstructure of all AAFA pastes. The reduced porosity, as well as refined pore structure was related to a higher degree of reaction of AAFA pastes at later curing age. More reaction products (aluminosilicate gel) were formed, filling the pore space, resulting in a

Figure 5 Pore size distribution of AAFA with different SiO_2 and Na_2O content at 7 and 28 days (cured at 40°C), derived from MIP.



denser matrix, corresponding to a higher compressive strength of AAFA pastes (Table 2).

The effect of SiO_2 in the activator

Figure 6a, b summarizes the total porosity and pore threshold diameter of AAFA pastes prepared with different SiO_2 content at 7 and 28 days (Na_2O content was kept constant at 1.5 mol/kg fly ash). Mixtures with a higher silica content presented a lower total porosity at 7 days (Fig. 6a). For mixtures with a silica content of 1.0 mol/kg fly ash (mixtures 1.0–1.5), the

decrease in the total porosity from 7 to 28 days was more pronounced than mixtures with a silica content of 1.5 mol/kg fly ash (mixtures 1.5–1.5). The same trend was observed for the gel pore threshold diameter of samples with different silica content (Fig. 6b).

The effect of Na_2O in the activator

The effect of the sodium content on the porosity and pore threshold diameter at 7 and 28 days are summarized in Fig. 6c, d (SiO_2 content was kept constant

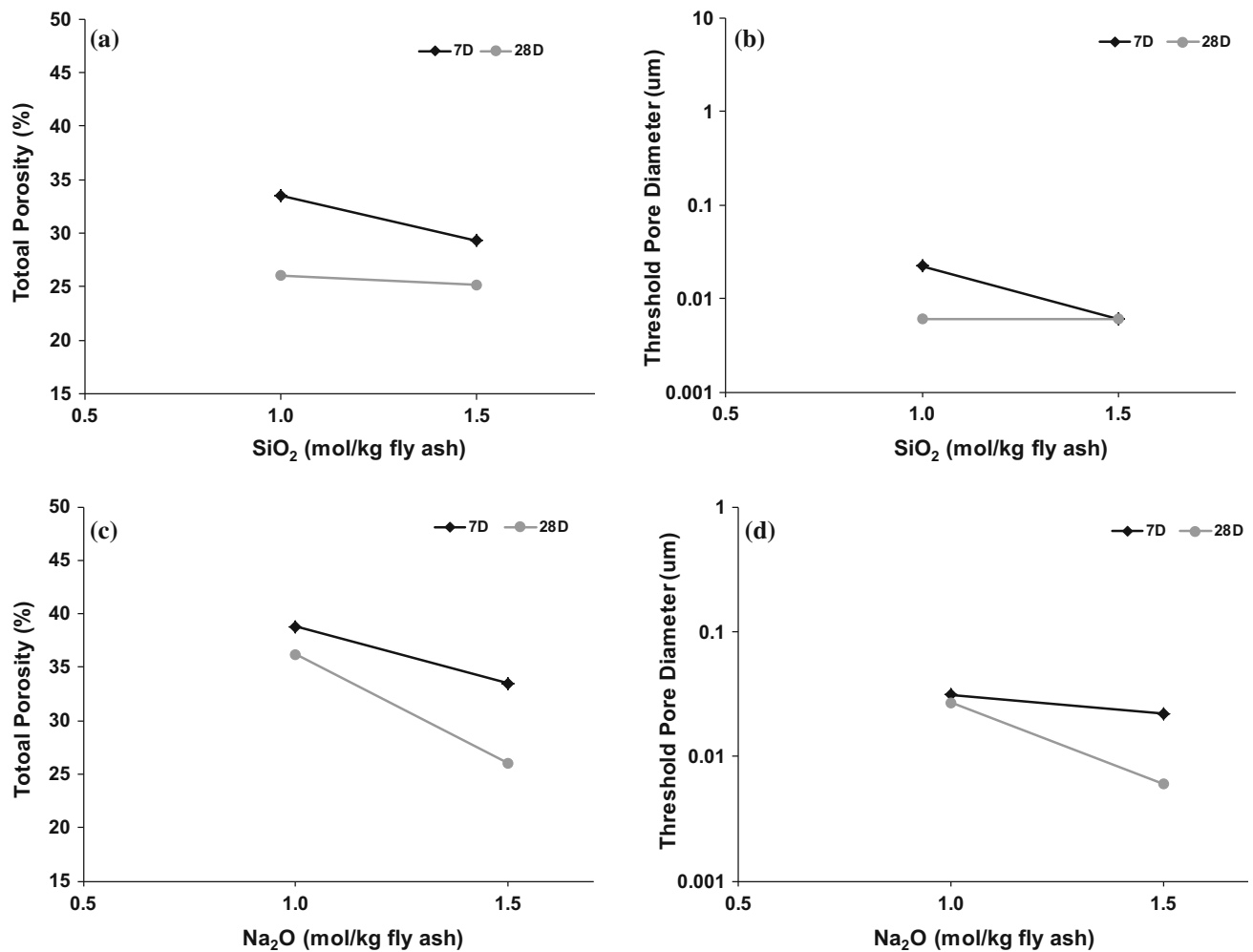


Figure 6 Total porosity (a, c) and gel pore threshold diameter (b, d) of AAFA pastes with different SiO₂ and Na₂O content, derived from MIP.

at 1.0 mol/kg fly ash). It was observed that the addition of more sodium led to a lower total porosity at 7 days, and this effect was more pronounced at 28 day (Fig. 6c). The same trend was found for the pore threshold diameter for AAFA samples with different sodium content, as shown in Fig. 6d.

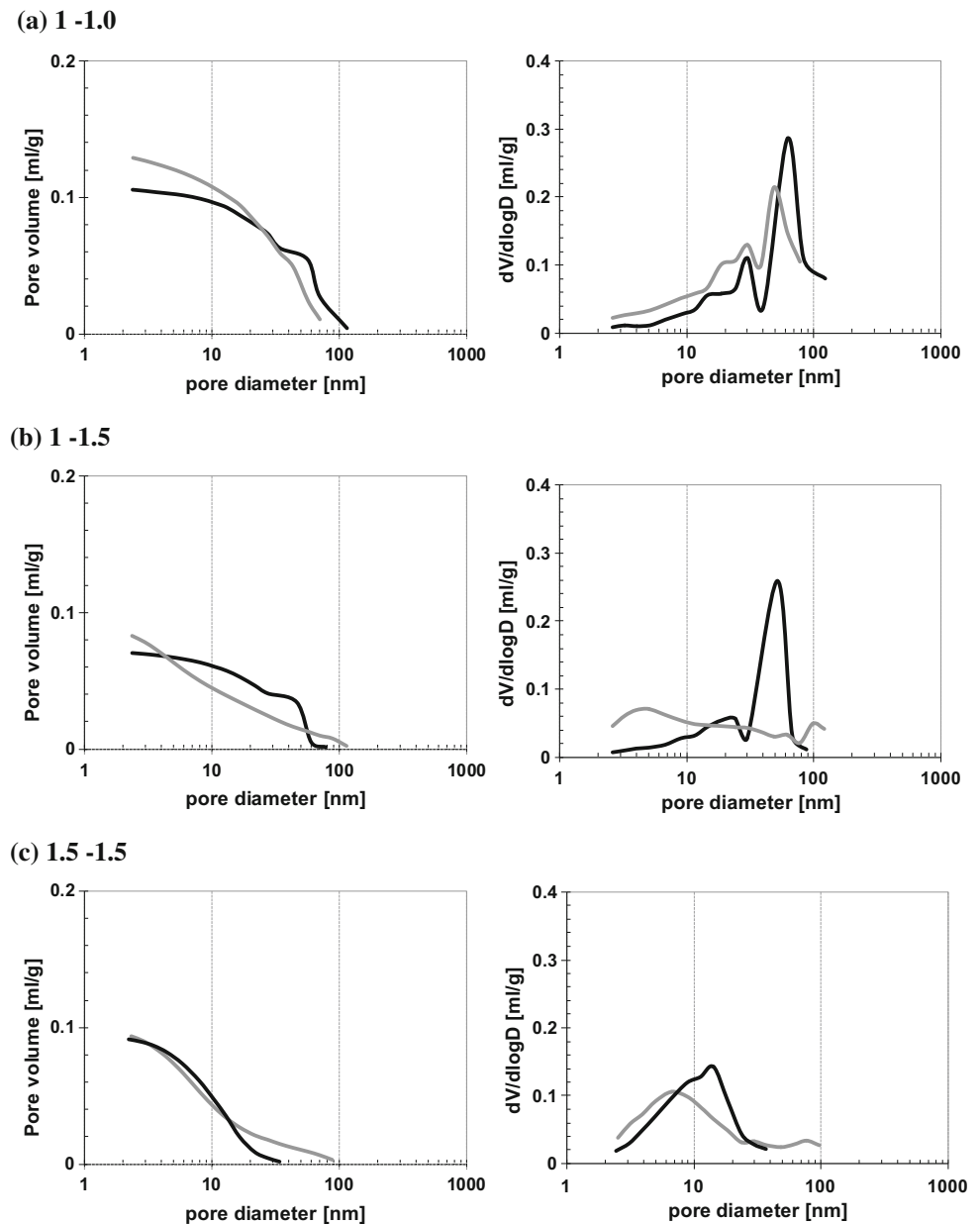
Pore structure of AAFA pastes determined by nitrogen adsorption

Figure 7 presents the pore size distribution of different AAFA mixtures derived from nitrogen adsorption tests. The pores between 2 and 100 nm can be detected by nitrogen adsorption, which technique gives more detailed information on gel pores in AAFA samples. It can be observed in Fig. 7 that the volume of pores increased with increasing age of the

AAFA samples. This result is expected, since the volume measured in the pore size range from 2 to 100 nm is primarily related to the gel phase. The quantity of aluminosilicate gel increased with age, causing an increase in the gel pore volume in the matrix.

The differential pore size distribution curves in Fig. 7 generally show two peaks. The pore diameter at these peaks varied with the silica and sodium content, as well as with the curing age. Mixtures with a higher silica content showed a lower pore diameter of the peak at 7 days, e.g. at around 50 nm for mixtures 1.0–1.5 (Fig. 7b) and 15 nm for mixtures 1.5–1.5 (Fig. 7c). At later age, mixtures 1.0–1.5, with a less silica content, had a denser gel pore structure than mixtures 1.5–1.5 at 28 days. Specimens with different

Figure 7 Pore size distribution of AAFA samples derived from the nitrogen adsorption tests at the curing ages of 7 and 28 days, respectively (cured at 40 °C).

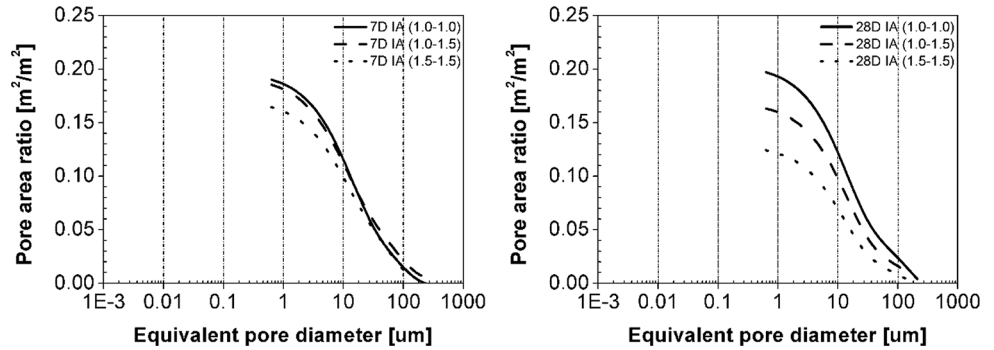


sodium content exhibited similar differential curves at the age of 7 days. Mixtures 1.0–1.0 and 1.0–1.5 showed similar peaks at 7 days, i.e. one peak between 50 and 60 nm, and the other peak between 20 and 30 nm. At 28 days, for mixtures with a higher sodium content, i.e. mixtures 1.0–1.5, the peak indicating the gel pores shifted to a lower pore diameter (5.1 nm) compared to that of mixtures with less sodium content, i.e. mixture 1.0–1.0. It indicates that the pores were finer for mixtures containing more sodium. This trend is in line with the results derived from MIP results.

Pore structure of AAFA pastes evaluated by image analysis

Figure 8 presents the pore size distribution of different AAFA samples derived from image analysis. It was observed that the total pore area ratio evaluated by image analysis method varied with the silica and sodium content in activator. Mixtures 1.5–1.5 showed the lowest total pore area ratio at the age of 7 days; and mixtures 1.0–1.5 and 1.0–1.0 presented similar total pore area ratio. At the age of 28 days, the total pore area ratio for mixtures 1.5–1.5 was still the smallest, followed by mixtures 1.0–1.5 and 1.0–1.0. In

Figure 8 Pore size distribution of AAFA samples derived from image analysis at the curing ages of 7 and 28 days, respectively.



addition, the decrease in the total pore area ratio of mixtures 1.5–1.5 was more pronounced than the other two mixtures. The results derived from image analysis method all indicated that the pores were finer for mixtures containing more silica and sodium content in activator at both 7 and 28 days.

Comparison of pore structure derived from image analysis and MIP

Figure 9 compares the pore size distribution of AAFA samples derived from image analysis and MIP. Table 3 summarized the porosity of AAFA from 0.01 to 1 µm, and from 1 to 150 µm, respectively. Because MIP is able to detect pores in a much larger pore size range, the total porosity derived from MIP measurement was significantly higher than that derived from image analysis (as shown in Fig. 9). From image analysis results, pores in the range of 1 µm to around 150 µm were found to be the dominant contributors to the total porosity, while the MIP results of the same mixtures showed that most of pores were in the range of 0.01 µm to about 1 µm (as shown in Table 3). Only a small volume of pores between 1 and 150 µm was detected by MIP. The large discrepancy between MIP and image analysis results indicated that the “ink-bottle effect” (larger

pores inside the specimen which can be intruded by mercury only through smaller pores [22, 24]) significantly affected MIP results of AAFA pastes. As observed from BSE image of AAFA (Fig. 1), the larger pores (from several micros to 100 µm) were formed by the dissolved fly ash particles or fly ash with a hollow core. These pores appeared as disconnected and were surrounded by the gels. The application of varied fly ash or different activators may result in different pore size distribution of AAFA, but the formation of the large pores mentioned above would be a common phenomenon in alkali-activated low-calcium fly ash, which was also reported in previous studies, presenting similar microstructures [25–27]. Lloyd et al. [25] found that these large pores were connected to the exterior of the specimens based on the results derived from Wood’s metal intrusion together with SEM image. During MIP measurement, mercury can only access these pores through finer pores, which in turn causes a significant “ink-bottle” effect, leading to an overestimation of the volume of fine pores and an underestimation of the volume of large pores. As a result, pores sizes obtained from MIP were two orders of magnitude smaller than those obtained by image analysis. Therefore, it seems that MIP technique cannot reflect the real pore size, especially the large pores in AAFA pastes.

Figure 9 Comparison of the pore size distribution curves derived from MIP and image analysis method for all investigated AAFA samples at 7 and 28 days.

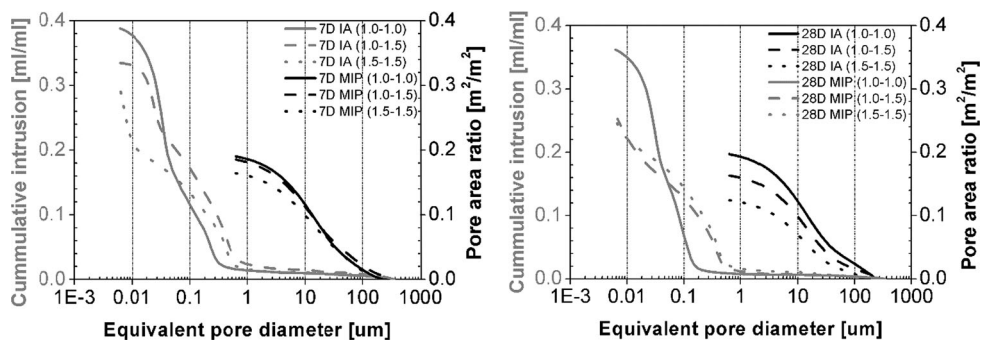


Table 3 The porosity of AAFA in different pore size range, derived from MIP and image analysis method

| Measurements | Mixture | Porosity | | | |
|----------------|---------|--------------------------|-------------------------|--------------------------|-------------------------|
| | | 7 days | | 28 days | |
| | | 0.01–1 μm (%) | 1–150 μm (%) | 0.01–1 μm (%) | 1–150 μm (%) |
| Image analysis | 1.0–1.0 | 0.45 | 18.55 | 0.41 | 18.87 |
| | 1.0–1.5 | 0.47 | 17.41 | 0.35 | 15.96 |
| | 1.5–1.5 | 0.42 | 16.01 | 0.32 | 12.10 |
| MIP | 1.0–1.0 | 36.44 | 1.00 | 34.30 | 0.63 |
| | 1.0–1.5 | 30.36 | 1.85 | 21.42 | 0.93 |
| | 1.5–1.5 | 20.13 | 1.14 | 20.33 | 1.01 |

The “ink-bottle” effect was also reported in previous studies [13, 22] on the characterization of pores in cement-based materials: they found that pore structure of cement paste derived from MIP and image analysis showed the same trend. However, in the present study, it is found that results derived from MIP and image analysis for alkali-activated fly ash presented different trend, as shown in Fig. 9 and Table 3, the results derived from image analysis demonstrated that mixture 1.5–1.5 presented the finest pore size in the pore size range of 0.1–150 μm compared to mixture 1.0–1.0 and 1.0–1.5 both at 7 and 28 days, while MIP results revealed that mixtures 1.0–1.0 presented the finest pore size distribution between 0.1 and 150 μm . This may be caused by the fact that the contact angle (known as θ in Eq. 1 in “Mercury intrusion porosimetry (MIP)” section) of mixture 1.5–1.5 and mixture 1.0–1.0 was different, while in this study, we adopted the same contact angle (132°) in the MIP measurement. To summarize, the pore size distribution derived from image analysis was more reliable to quantify large pores ($> 1 \mu\text{m}$) in AAFA pastes. Nevertheless, it should be noted that image analysis may overestimate the large pores in AAFA by adding the pores inherent to fly ash particles into the total porosity. These pores normally exist in hollow fly ash particles and were not accessible to the exterior. They become visible only when the sample is grinded for SEM observation. This error is estimated to be lower than 2% of the total volume of fly ash.

Comparison of the pore structure derived from MIP and nitrogen adsorption

Figure 10 compares the differential pore size distribution curves derived from MIP and nitrogen adsorption tests for AAFA samples at 7 and 28 days.

Table 4 summarized the critical pore size of gel pores and capillary pores in AAFA, derived from these two methods. One clear difference is that nitrogen adsorption measurements generally revealed two peaks in the gel pore range of AAFA samples (dashed lines in Fig. 10), while in MIP tests only one peak appeared indicating the gel pores (solid lines in Fig. 10). In addition, these peaks appeared at different pore diameters and with different peak intensities (Fig. 10 and Table 4). For example, mixtures 1.0–1.0 showed one peak at 33.9 nm at 7 days in MIP results (Table 4), while nitrogen adsorption results indicated two peaks at 24.1 and 61.9 nm (Table 4). These differences may be related to different mediums (mercury compared to nitrogen) and principles (liquid intrusion compared to gas adsorption) used in MIP and nitrogen adsorption measurements. Another reason may come from the high pressure used during MIP measurements, which may cause damage to the pore structure, especially at smaller pore diameters when higher pressures are applied. This may lead to the appearance of only one peak corresponding to the gel pores in MIP results. Despite the differences between MIP and nitrogen adsorption results for different AAFA samples, these two methods give similar trends: samples with a higher silica content presented a finer pore structure at early curing age, whereas samples with a higher sodium content developed a finer pore structure at later age.

Reaction degree derived from image analysis

Using image analysis method introduced in “Image analysis based on environmental scanning electron microscope (ESEM)” section, the degree of reaction of AAFA pastes was calculated based on the area ratio of unreacted fly ash particles, as described in Fig. 11.

Figure 10 Comparison of the pore size distribution curves derived from MIP and nitrogen adsorption (N₂) tests for all investigated AAFA samples at 7 and 28 days.

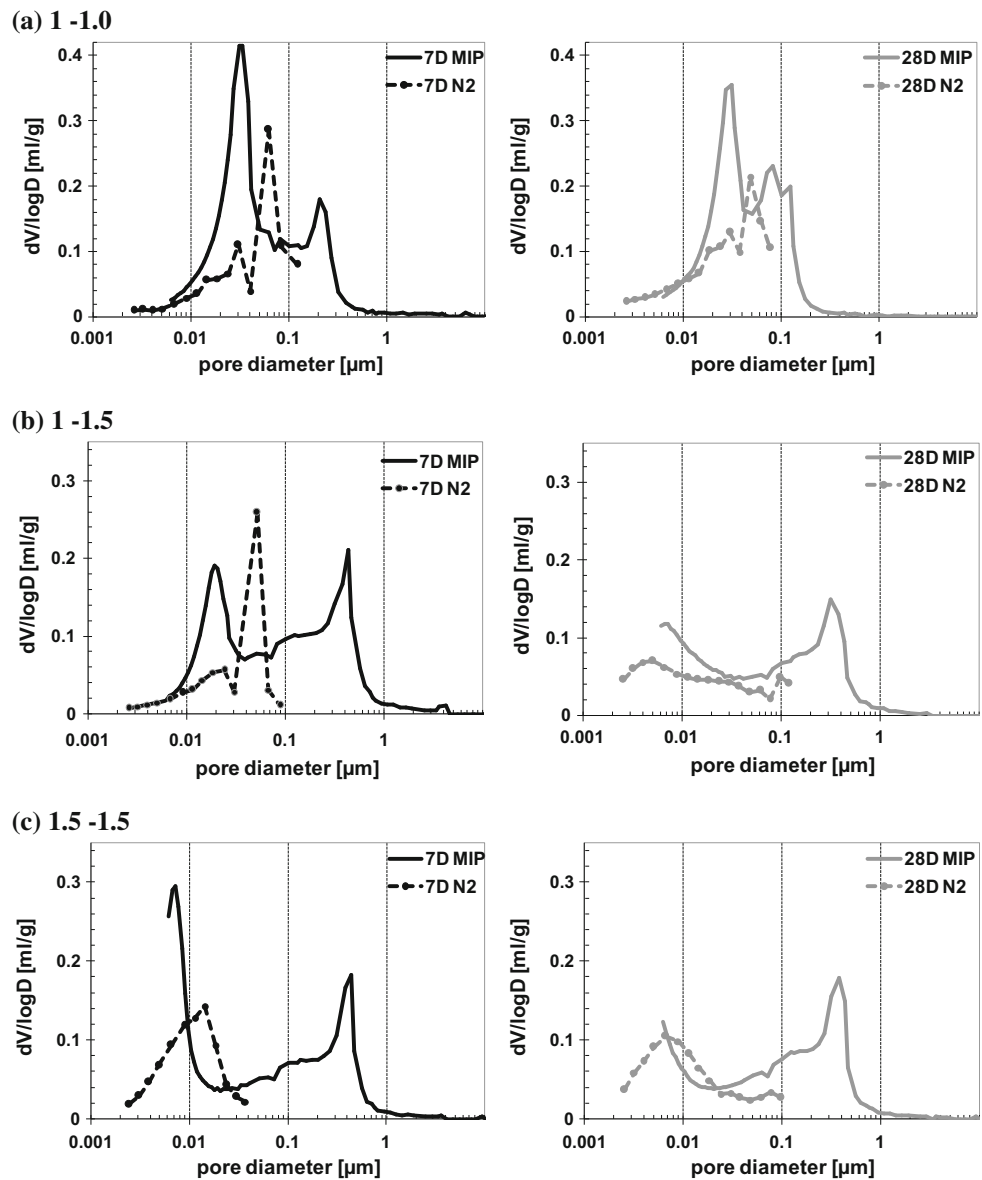


Table 4 The critical pore size of the gel pores and capillary pores in AAFA, derived from MIP and N₂ adsorption

| Measurements | Mixture | Critical pore size (nm) | | | |
|---------------------------|---------|-------------------------|-----------------|-----------|-----------------|
| | | 7 days | | 28 days | |
| | | Gel pores | Capillary pores | Gel pores | Capillary pores |
| MIP | 1.0–1.0 | 33.9 | 203.3 | 31.2 | 82.0 |
| | 1.0–1.5 | 20.5 | 436.4 | < 6.0 | 314.9 |
| | 1.5–1.5 | 7.0 | 380.9 | < 6.0 | 380.9 |
| N ₂ adsorption | 1.0–1.0 | 24.1/61.9 | – | 30.1/48.4 | – |
| | 1.0–1.5 | 23.9/51.9 | – | 5.1 | – |
| | 1.5–1.5 | 14.3 | – | 6.7 | – |

In general, a lower Na₂O content led to a lower reaction degree of AAFA samples, i.e. mixtures 1.0–1.5 presented a higher reaction degree than

mixtures 1.0–1.0 (Fig. 11). As described in previous studies [1], the alkali activation process of fly ash involved five steps: dissolution, speciation

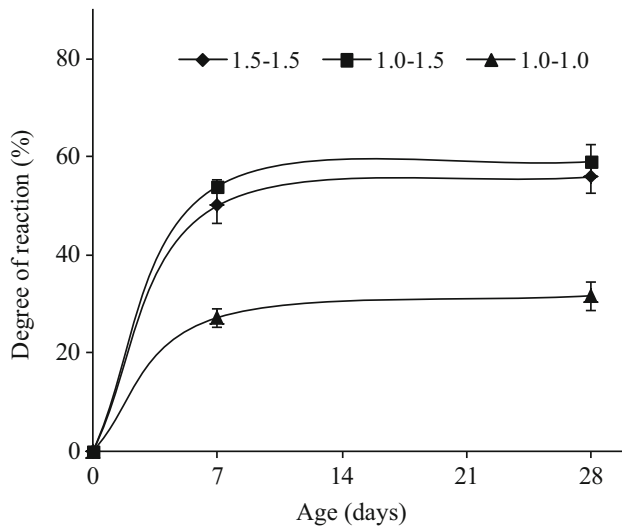


Figure 11 Degree of reaction of AAFA mixtures with different SiO_2 and Na_2O content, derived from image analysis.

equilibrium, gelation, reorganization and polymerization. Alkali cations (expressed as Na_2O content here) in the activating solutions were regarded to have two effects: first, the addition of Na_2O increased the pH in the activating solution. A high content of OH^- ions increased the dissolution rate of fly ash particles, breaking Si–O–Si and Si–O–Al bonds into small silicon and aluminium species [1]. These small ionic species may form a coagulated structure, resulting in a three-dimensional aluminosilicate gel. Second, alkali cations balanced the electrical charge in the three-dimensional Si and Al structure [28], being incorporated into the gel. As a result, for AAFA system with a higher Na_2O content, the dissolution rate of fly ash particles was higher, leading to a higher reaction degree. Correspondingly, mixtures with a higher sodium content presented a lower total porosity and finer pore structure distribution, resulting in a higher mechanical strength (Table 2).

SiO_2 content in the activating solutions affects the reaction in a different way. Samples with higher silica content had lower degree of reaction, i.e. mixtures 1.5–1.5 presented a lower degree of reaction than mixtures 1.0–1.5 both at 7 and 28 days. According to Criado et al. [29], an increase in silica content led to a higher degree of silicate polymerization in activating solutions. For activating solution with a higher SiO_2 content, the fraction of monomeric and dimeric silicates species decreased, while trimer units of silicate species grew. Monomeric and dimeric silicates can directly react with the aluminate anions, forming

an initial aluminosilicate gel in a fairly short time, while silicate trimers reacted relatively slowly with aluminate anions that were dissolved from the fly ash [30]. The phases formed with a high silica addition were fairly stable [29], which hampered the subsequent reaction of fly ash particles, resulting in a lower reaction degree. On the other hand, silica was incorporated in the gel, leading to a dense microstructure. Therefore, the pore structure of mixtures 1.5–1.5 was finer than mixtures 1.0–1.5 at 7 days. This finer pore structure of mixtures 1.5–1.5 correlates well to its higher compressive strength at 7 days (Table 2), although the degree of reaction of mixtures 1.5–1.5 was lower. At 28 days, mixtures 1.0–1.5 presented a denser gel pores than mixtures 1.5–1.5. Thus, the compressive strength of mixtures 1.0–1.5 was higher than that of mixtures 1.5–1.5 at 28 days (Table 2).

Conclusions

In this study, the pore structure of AAFA pastes with different SiO_2 and Na_2O content in activator was evaluated by MIP, nitrogen adsorption and image analysis method. The results obtained from different techniques were compared. It was found that due to a significant ink-bottle effect, MIP measurement cannot provide correct pore structure information of AAFA pastes by overestimating the volume of fine pores ($< 1 \mu\text{m}$) and underestimating the volume of large pores ($> 1 \mu\text{m}$). Pore diameters derived from MIP were two orders of magnitude smaller than the pore sizes revealed by image analysis. Different peaks (corresponding to different critical pore diameter of gel pores) were characterized by MIP and nitrogen adsorption, while the comparison of equal handled samples reflected the same trend. Image analysis technique was believed to give reliable and consistent results of the pore size distribution of large pores, as well as the degree of reaction of fly ash in AAFA pastes.

Acknowledgements

The authors thank the China Scholarship Council for the financial support to the first author's study in The Netherlands. We also thank the National High Technology Research and Development Program ("863 Program", SS2015AA030801), National Natural

Science Foundation of China (51402057, 51561135012), Science and Technology Project of Guangdong Province (2016B05051004), Guangzhou Education Bureau Foundation (1201610460), State Key Laboratory of Silicate Materials for Architectures Foundation (SYSJJ2017-05), Pearl River S&T Nova Program of Guangzhou (201506010004) and Australian Research Council Discovery Project (1006016) for funding the project. We would like to thank Professor Klaas van Breugel for his ultimate support and guidance to the project.

References

- [1] Provis JL, Van Deventer J (2009) Geopolymers: structure, processing, properties and industrial applications. Woodhead Publ. Limited, Sawston
- [2] Duxson P, Provis JL, Lukey GC, Van Deventer JSJ (2007) The role of inorganic polymer technology in the development of 'green concrete'. *Cem Concr Res* 37:1590–1597
- [3] Provis JL, Deventer JSJV (2014) Alkali activated materials. Springer, Dordrecht
- [4] Romagnoli M (2015) Handbook of alkali-activated cements, mortars and concretes
- [5] Aligizaki KK (2005) Pore structure of cement-based materials: testing, interpretation, and requirements. CRC Press, Boca Raton
- [6] Diamond S (2000) Mercury porosimetry: an inappropriate method for the measurement of pore size distributions in cement-based materials. *Cem Concr Res* 30:1517–1525
- [7] Ma H (2014) Mercury intrusion porosimetry in concrete technology: tips in measurement, pore structure parameter acquisition and application. *J Porous Mater* 21:207–215
- [8] Zeng Q, Li K, Fen-Chong T, Dangla P (2012) Analysis of pore structure, contact angle and pore entrapment of blended cement pastes from mercury porosimetry data. *Cem Concr Compos* 34:1053–1060
- [9] Joyner LG, Barrett EP, Skold R (1951) The determination of pore volume and area distributions in porous substances. II. Comparison between nitrogen isotherm and mercury porosimeter methods. *J Am Chem Soc* 73:373–380
- [10] Gerhardt R (1988) As review of conventional and non-conventional pore characterization techniques. *Mrs Online Proceedings Library Archive*, 137
- [11] Aligizaki K (2005) Pore structure of cement-based materials: testing interpretation and requirements. Taylor & Francis, London
- [12] Haha MB, Weerdt KD, Lothenbach B (2010) Quantification of the degree of reaction of fly ash. *Cem Concr Res* 40:1620–1629
- [13] Guang YE (2003) Experimental study and numerical simulation of the development of the microstructure and permeability of cementitious materials. *J Colloid Interface Sci* 262:149–161
- [14] Ma Y, Hu J, Ye G (2012) The effect of activating solution on the mechanical strength, reaction rate, mineralogy, and microstructure of alkali-activated fly ash. *J Mater Sci* 47:4568–4578. <https://doi.org/10.1007/s10853-012-6316-3>
- [15] Scrivener K, Snellings R, Lothenbach B (2016) A practical guide to microstructural analysis of cementitious materials. CRC Press, Boca Raton
- [16] Ye G (2003) The microstructure and permeability of cementitious materials. Delft University of Technology, Delft
- [17] Washburn EW (1921) The dynamics of capillary flow. *Phys Rev* 17:273
- [18] Ellison AH, Klemm R, Schwartz AM, Grubb L, Petrash DA (1967) Contact angles of mercury on various surfaces and the effect of temperature. *J Chem Eng Data* 12:607–609
- [19] Gerhardt R (1989) A review of conventional and non-conventional pore characterization techniques. *Mater. Res. Soc. Symposium Proceedings*, 137, Pore structure and permeability of cementitious materials, Cambridge Univ Press, pp 75–82
- [20] Barrett EP, Joyner LG, Halenda PP (1951) The determination of pore volume and area distributions in porous substances. I. Computations from nitrogen isotherms. *J Am Chem Soc* 73:373–380
- [21] Scrivener K, Füllmann T, Gallucci E, Walenta G, Bermejo E (2004) Quantitative study of Portland cement hydration by X-ray diffraction/Rietveld analysis and independent methods. *Cem Concr Res* 34:1541–1547
- [22] Diamond S, Leeman ME (1994) Pore size distributions in hardened cement paste by SEM image analysis. *Mrs Proceedings*, 370
- [23] Ridler TW, Calvard S (2007) Picture thresholding using an iterative selection method. *IEEE Trans Syst Man Cybern* 8:630–632
- [24] Lange DA, Jennings HM, Shah SP (1994) Image analysis techniques for characterization of pore structure of cement-based materials. *Cem Concr Res* 24:841–853
- [25] Lloyd RR, Provis JL, Smeaton KJ, van Deventer JSJ (2009) Spatial distribution of pores in fly ash-based inorganic polymer gels visualised by Wood's metal intrusion. *Microporous Mesoporous Mater* 126:32–39
- [26] Ismail I, Bernal SA, Provis JL, Nicolas RS, Hamdan S, Deventer JSJV (2014) Modification of phase evolution in

- alkali-activated blast furnace slag by the incorporation of fly ash. *Cem Concr Compos* 45:125–135
- [27] Das S, Yang P, Singh SS, Mertens JCE, Xiao X, Chawla N, Neithalath N (2015) Effective properties of a fly ash geopolymer: synergistic application of X-ray synchrotron tomography, nanoindentation, and homogenization models. *Cem Concr Res* 78:252–262
- [28] Criado M, Fernandez-Jimenez A, de la Torre AG, Aranda MAG, Palomo A (2007) An XRD study of the effect of the $\text{SiO}_2/\text{Na}_2\text{O}$ ratio on the alkali activation of fly ash. *Cem Concr Res* 37:671–679
- [29] Criado M, Fernandez-Jimenez A, Palomo A, Sobrados I, Sanz J (2008) Effect of the $\text{SiO}_2/\text{Na}_2\text{O}$ ratio on the alkali activation of fly ash. Part II: Si-29 MAS-NMR Survey. *Microporous Mesoporous Mater* 109:525–534
- [30] Rees CA, Provis JL, Lukey GC, van Deventer JSJ (2007) In situ ATR-FTIR study of the early stages of fly ash geopolymer gel formation. *Langmuir* 23:9076–9082